Title	Nondestructive characterization of fusion and plasma activated wafer bonding using mesa and recess structures
Author(s)	Varpula, Aapo; Suni, Tommi; Dekker, James R.
Citation	ECS Journal of Solid State Science and Technology. ECS. Vol. 4 (2015) No: 2, P42 - P52
Date	2015
URL	http://dx.doi.org/10.1149/2.0121502jss
Rights	© The Electrochemical Society, Inc. 2014. All rights reserved. Except as provided under U.S. copyright law, this work may not be reproduced, resold, distributed, or modified without the express permission of The Electrochemical Society (ECS). The archival version of this work was published in (see above).

Nondestructive Characterization of Fusion and Plasma Activated Wafer Bonding Using Mesa and Recess Structures

Aapo Varpula,[z] Tommi Suni, and James R. Dekker

VTT Technical Research Centre of Finland, 02044 VTT, Espoo, Finland

We present two methods for characterization of wafer bonding. They are based on recess and mesa bond test structures with various shapes, measurement of unbonded regions using scanning acoustic microscopy (SAM), and image analysis. The first method maps locally the surface energy across the bonded wafers using the measured deformations around these structures and the finite element method (FEM). The FEM analysis is supported by analytical modeling. The second method uses the measured bonding probabilities of 10–19 nm deep recess bond test structures in investigation of surface interactions and in determination of the average of the surface energy at the wafer level. The present methods and proposed optimized test structures allow the evaluation of surface cleans without destructive, off-line methods such as the crack-opening method, which is employed as a reference. The methods are utilized in the investigation of the effect of O_2 and N_2 plasma activation and the dilution and temperature of Standard Clean 1 on Si/SiO_2 direct bonding. The results from both methods correlate with each other. The bond strength of the annealed wafers is observed to increase in the order 1) O_2 plasma, 2) standard SC1 at 65°C, 3) N_2 plasma, and 4) dilute SC1 at 45°C.

Wafer bonding is an essential component of the semiconductor industry.[1-3] It allows wafer level packaging, 3D integration of diverse devices, and manufacturing of silicon-on-insulator (SOI) wafers needed as substrates for microelectromechanical systems (MEMS) and high performance microelectronic and photonic devices.[1] Perhaps the most common bonding process used, especially for SOI production, is fusion wafer bonding which usually follows the procedure:[1,2] First the wafer surfaces are prepared in a cleaning treatment and then the wafers are joined together in vacuum at room temperature. The final bond strength is obtained during annealing at high temperatures. In plasma-activated wafer bonding[3,4] the wafers are pretreated in plasma. This allows high bond strengths to be obtained at lower annealing temperatures.

Wet cleaning is an essential step required before fusion bonding of hydrophilic silicon wafers can succeed. The chemistry of Standard Clean 1 (SC1) is a convenient and highly effective method. Numerous early studies such as Refs. 5–8 all used SC1 as part of the standard wafer cleans before wafer bonding. There are three main objectives of the SC1 clean. Firstly, the importance of a hydrophilic surface terminated with hydroxyl groups, readily provided by a basic solution such as SC1, to bonding has long been noted by Maszara et al.,[9] and elucidated in detail by Tong and Gösele.[8] Secondly, the SC1 clean removes organic contaminants which are known to interfere with bonding reactions.[6] Finally, the SC1 clean is very effective at removing particles from wafer surfaces as described in detail by Itano and Kezuka.[10] As an additional criteria, roughening of the surface can be minimized with proper dilution of the cleaning solution.[9,11] The SC1 clean meets these requirements for silicon wafers and for wafers with thermal oxide.

Once wafers are bonded and annealed, their bond strength is often characterized destructively by measuring their bonding energy as the energy required to form the surfaces created when the bonded wafers are pulled apart.[8,12] The crack-opening method or the couple-cantilever-beam test method[8,12] is a common destructive method which measures the bond strength. Obviously, if bonding energies are sufficiently high, then 3D fracture, in which the fracture surface departs from the bonded interface, will result and precise quantification of the surface energy is difficult to obtain.[12] Nevertheless, a high surface energy is considered a prerequisite for good quality fusion bonding of hydrophilic silicon and oxide wafers. This surface energy, at the time of bonding, is determined by the pre-bond cleaning treatment.[3,12]

Non-destructive methods for characterization of bond interfaces have also been developed: scanning acoustic microscopy (SAM),[8] infrared (IR) transmission imaging,[8] and scanning IR interferometry.[13] If both of the bonded wafers are made of single-crystalline materials (e.g. in Si to Si bonding), then X-ray topography[8] can be used as well. In general, these methods give a qualitative measure of the bonding process, such as void fraction or yield, but they do not measure the bond strength.

These imaging methods, however, can be used to determine the bond strength, when they are combined with bond test structures fabricated on wafers. Vallin and his coworkers[12] reviewed a wide range of different bond-strength measurement techniques, including some bond strength test structures which utilized predefined surface steps. Generally mesas and recesses can be used as bond strength test structures. Mesa and recess type bonding test structures are sketched in Fig. 1. In this paper we use both mesa and recess bonding test structures with various shapes to evaluate the surface energy of the bonded wafers at the time of contact. Previously mesa test structures were utilized in both direct[14,15,16] and anodic bonding.[17,18] To the best of our knowledge recess test structures were utilized only in anodic bonding[19,20,21] when we published our first indicative results in 2012.[22]

We analyze the bonding test structures on wafers with SC1 and plasma activation pre-bonding treatments by SAM. We present two new methods where the SAM images of the bonded wafers can be evaluated either locally, when accompanied by FEM analysis similarly as in the previous studies, or at wafer level, by measuring the probability that shallow recesses of a certain size will spontaneously bond. The former method allows mapping of the local apparent surface energy across the wafer, and the latter the determination average surface energy at the wafer level separately from the measured bond test structure statistics. Our results show good correlation between the two methods. Although the methods measure the surface energy of the activated surfaces before bonding, it is shown that in case of SC1 activation the measured surface energy correlates also well with the final bond strength of the annealed wafer pair. In addition, we show that the new statistical method can be used in studying the interaction between the wafers during the bonding process.

The local surface energy is determined by measuring the unbonded region next to the patterned step. This data is fit to the FEM models to give a surface energy value. The FEM models are validated by analytical modeling. Most of the previous studies utilized steps of the order of 100 nm or higher and either analytical[14,15,18,23,24] or FEM models.[17] Martini et al.[16] combined analytical and FEM models in

[z]E-mail: aapo.varpula@vtt.fi
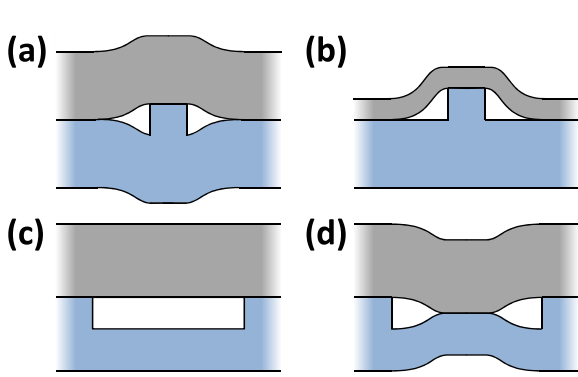
Figure 1. Schematic pictures of (*a–b*) mesa and (*c–d*) recess bonding test structures. The top wafer is much thinner than the bottom wafer in (b), and thicknesses of the wafer are equal in (a). The recess cavity can be either (*c*) unbonded or (*d*) bonded. The heights of the mesas and the depths of the recesses are highly exaggerated: the practical vertical dimensions are several orders of magnitude smaller than the wafer thicknesses.

the study of surface steps with height 9–400 nm. In this article we utilize shallow, 10–19 nm high, steps, and present analytical models for surface steps and circular mesas and recesses and compare them with our FEM simulations and previous models.

Finally, based on the results obtained with our methods, we propose test patterns that allow in-line monitoring of the surface clean effectiveness on process wafers.

**Theory: Extraction of Surface Energy with Bond Test Structures**

In this section we show theoretically how the surface energies of bonded wafer surfaces can be extracted using the measured geometrical dimensions of the wafer deformations around the bond test structures. We use the same procedure to calculate the surface energy from the deformed test structures as Wan[23] and Pasquariello[15] and their co-workers. It is assumed that the cracks associated with the test structures are of the mode I, i.e. opening mode, where a tensile stress is normal to the plane of the crack. We calculate the surface energies using both analytical formulas based on the thin plate theory[25] and COMSOL Multiphysics FEM simulation software. In both models we assumed that silicon is isotropic with the modulus of the elasticity $E = 170$ GPa and Poisson's ratio $\nu = 0.28$.

In the analytical calculation and FEM simulation the surface energy is calculated from the Griffith–Irwin mechanical-release rate as[15,23]

$$\gamma = -\frac{1}{2} \cdot \frac{dU}{dA}, \qquad [1]$$

where U is the mechanical energy, i.e. the work equal to the total strain energy of the system, and A is the area of the deflected surface, i.e. the crack area. In the FEM simulations U is obtained by numerical integration of the strain energy density and γ by numerical differentiation and subsequent averaging filtering.

Surface step.— Although the calculations are performed for infinitely wide surface steps, we assume that the results can also be used for real surface step structures, such as large square recesses, as long as the unavoidable lateral edges are far from the studied part of the surface step. The local strain energy of the wafers near a surface step can be calculated analytically with the formulas derived for wide elastic straight beams.[25] The case discussed here is shown in Fig. 2. The fixed boundary condition (i.e. no deflection or rotation is allowed)[25] is used at the right end of beam. The left end of the beam is guided (i.e. the slope of the beam is zero at this end and no rotation or shear is allowed),[25] which also acts as a symmetry boundary condition. The force F_{step} is acting on the guided end of the beam. In general, the force needed to deform the beam to an arbitrary deflection of y is
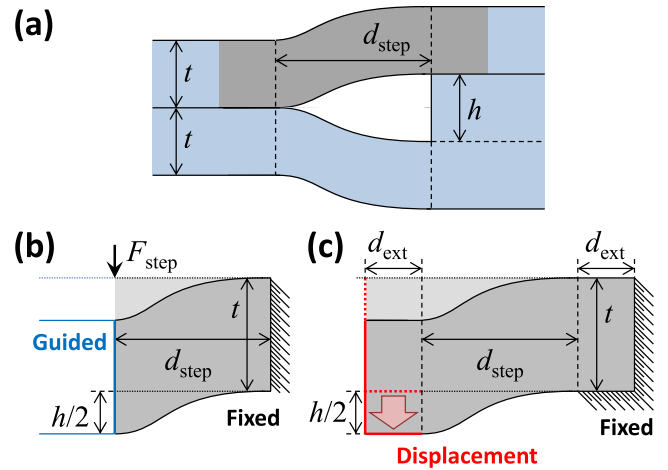
Figure 2. (*a*) Schematic picture of a surface step test structure with height h. d_{step} is the length of the unbonded region near the surface step and t is the wafer thickness. Due to the symmetry the highlighted area needs only to be considered in the calculations. (*b,c*) Geometry and boundary conditions used in the calculation of surface energies: (*b*) analytical and (*c*) FEM model. The pictures are not in scale.

given by (cf. Ref. 25)

$$F_{step}(y) = \frac{wE't^3y}{d_{step}^3}, \qquad [2]$$

where t is the wafer thickness, d_{step} and w are the length and width of the beam, respectively, $E' = E/(1 - \nu^2)$, E is the modulus of the elasticity of the material, and ν is Poisson's ratio of the material. Here the length of the beam d_{step} corresponds to the length of the unbonded region near the surface step.

The mechanical energy needed to deflect two beams by $h/2$, where h is the step height, can be written as

$$U_{step} = 2 \int_0^{h/2} F_{step}(y)\,dy = \frac{wE't^3h^2}{4d_{step}^3}. \qquad [3]$$

Using Eqs. (1) and (3) and the formula $A = d_{step}w$ gives the surface energy as

$$\gamma_{step} = \frac{3E't^3h^2}{8d_{step}^4}. \qquad [4]$$

This formula is similar to the formula obtained by Hiller[24] and Horning et al.,[14] although they did not use the correction factor for wide beams, $1/(1-\nu^2)$.[25] In addition, Horning et al. assumed that one bonded wafer was much thinner than the other, and only the thinner wafer deflects. Martini et al.[16] derived an analytical model for the case of short unbonded regions ($d_{step} < 2t$) using analytical formulas describing the elastic strain fields around a straight dislocation.[26] Using their model the surface energy can be written as (cf. Ref. 16)

$$\gamma_{step}^M = \frac{E'h^2}{8\pi d_{step}}. \qquad [5]$$

The 2D geometry and the boundary conditions of the FEM simulation are shown in Fig. 2b and 2c. As in the analytical model, one end of the structure is fixed, but the other end is displaced downwards by $h/2$. The simulated geometry has extensions with the lengths of $d_{ext} = 2d_{step}$ at the ends of the beam. These extensions allow the slight deformations of the wafers in the surrounding regions to be modeled. The mesh of the FEM simulation is rectangular and consists of 28,800 elements. The mesh is denser near the bottom and the ends of the beam. Because the FEM simulation yields a value for U/w, but
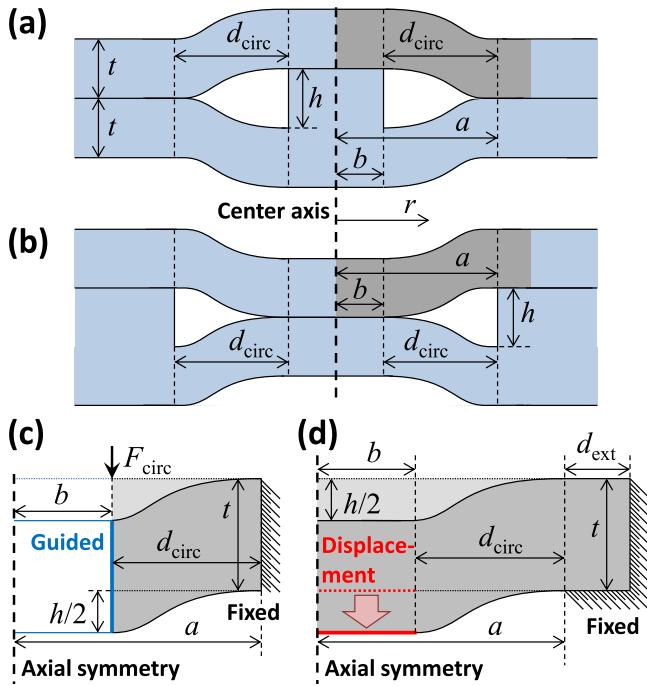
Figure 3. (a,b) Schematic picture of (a) a circular mesa with height h and (b) a circular recess with depth h. $d_{circ} = a - b$ is the radial width of the unbonded rim. Due to the symmetry the highlighted areas need only to be considered in the calculations. (c,d) Geometry and boundary conditions used in the calculation of surface energies: (c) analytical and (d) FEM model. The pictures are not in scale. In (d) the FEM model of a recess structure is shown. The FEM model of a mesa structure is the same except the displacement is upwards. The pictures are not in scale.

not for U, Eq. (1) is utilized in the form

$$\gamma_{step} = -\frac{1}{2} \cdot \frac{dU}{dA} = -\frac{1}{2} \cdot \frac{d}{dd_{step}}\left(\frac{U}{w}\right), \qquad [6]$$

where the formula $A = d_{step}w$ was used.

Circular mesa and recess.— The local strain energy near circular mesas and recesses shown in Fig. 3 can be calculated analytically with the formulas derived for annular plates.[25] In the case shown in Fig. 3c the inner edge of the annular plate (at $r = b$) is guided and the outer edge (at $r = a$) is fixed. A line load is applied uniformly on the inner edge. The total force corresponding to this line load depends on an arbitrary deflection of y by (cf. Ref. 25)

$$F_{circ}(y) = \frac{\pi}{6} \cdot \frac{b}{a} \cdot \frac{E't^3 y}{a^2 C}, \qquad [7]$$

where $C = b(1 - [b/a]^2\{4(\ln b/a)^2/[1 - (b/a)^2] + 1\})/8a$. In the case of the recess test structure a is the radius of the circular recess and b is the radius of the bonded region inside the recess. In the case of the mesa test structure b is the radius of the circular mesa and a is the radius of an area which includes the mesa and the deflected region. The radial width of the unbonded rim around a mesa test structure and inside a recess test structure is $d_{circ} = a - b$.

The mechanical energy needed to deflect two of these kinds of annular plates by $h/2$ can be written as

$$U_{circ} = 2\int_0^{h/2} F_{circ}(y)\, dy = \frac{\pi}{24} \cdot \frac{b}{a} \cdot \frac{E't^3 h^2}{a^2 C}. \qquad [8]$$

Using Eqs. (1) and (8) and the formula $A = \pi a^2$ gives the surface energy as

$$\gamma_{circ} = \frac{b}{a} \cdot \frac{E't^3 h^2}{32a^4 C}\left(1 + \frac{D}{3C}\right), \qquad [9]$$

where $D = [(b/a)^3 \ln b/a]\{(b/a)^2 \ln (b/a)/[1 - (b/a)^2] + 3\ln (b/a)/2 + 1\}/[1 - (b/a)^2] + 3(b/a)^3/8 - b/8a$.

The 2D geometry and the boundary conditions of the FEM simulation are shown in Fig. 3d. The outer edge of the plate is fixed. In the model for a recess structure (Fig. 3d) the part of the bottom is displaced downwards by $h/2$. In the model of a mesa structure the part of the bottom is displaced upwards by $h/2$. As before, the simulated structure is extended by the radial width $d_{ext} = 2a$. The mesh of the FEM simulation is rectangular and consists of 26,400–31,200 elements, depending on the dimensions. The mesh is made denser near the bottom of the plate and the inner edge of the displaced region.

Modeling considerations.— In the analysis the thickness t of the both of the bonded wafers are assumed to be equal. The fact that the other wafer has 10–20 nm deep recesses does not affect the analysis, since t is usually in the range of hundreds of micrometers. In direct wafer bonding of silicon wafers, silicon oxide is often employed at the bond interface. The effect of the thin (< 1 μm) silicon oxide layer at the bonding interface and possible structural defects near high stress points are neglected in the model. Furthermore, the effect of the external atmospheric pressure on the deformation of the vacuum-sealed test structures is not considered. Our FEM simulations have shown this effect to be negligible in the test structures utilized in this work. For larger membranes the analytical model by Wan et al.[23] can be used to estimate the effect of the external pressure.

Compared to destructive methods, such as the crack-opening method, the bond test structures estimate the surface energies of the bonded wafer surfaces, when they are brought into contact.[12] Any subsequent processing steps which alter the bond strength will not be detected by the bond test structures, unless their deformations change accordingly. To emphasize this crucial difference between the surface energy given by the bond test structures and that given by the destructive methods, we introduce the term apparent surface energy, which is the surface energy indicated by our analysis of the bond test structures. In the case of direct bonding of silicon wafers, this apparent surface energy seems to be determined by the conditions of the wafer surfaces during contact (see the results section for further discussion).

Experimental

Bonding test structure and sample fabrication.— The layouts of the bonding test structures used in the experiments are sketched in Fig. 4. These layouts were reproduced multiple times on a wafer. The wafer-level arrangements used in the experiments are shown in Fig. 5.

The fabrication process of the 675 μm thick 150 mm silicon wafers is sketched in Fig. 6. The cap wafer has 500 nm of thermal wet oxide (Fig. 6a). The recesses and mesas were fabricated on the handle wafers by first growing 500 nm of thermal oxide (Fig. 6a), and patterning it using photolithography and buffered HF etching (Fig. 6b). Then, a thin dry-oxide layer was grown on the handle wafers (Fig. 6c). Finally, all the oxide was etched away in 49 % HF (Fig. 6d).

The thickness of the thin dry-oxide layer was varied from 24 nm to 56 nm so that the final depths of the recesses of the test structures varied from 10 nm to 19 nm. This recess depth defines the value of h in all test structures (see the theory section). The depths of the recess were estimated by combining results from reflectometry using a FilmTek 2000M and profilometry using a Veeco Dektak M6. Based on the reflectometry data an uniformity of 3 % was estimated for the recess depth across the wafer.

Prior to bonding the fusion bonded wafers were cleaned in SC1 using either dilute or standard dilution at the temperature of either 45 °C or 65 °C. The dilution of the standard SC1 mixture is 1:1:5 of ammonia (25 % solution), H_2O_2 (30 % solution), and H_2O. The dilute SC1 mixture is 1:4:20. The plasma bonded wafers were first cleaned in the standard SC1 at 45 °C and then activated in either N_2 (power 230 W) or O_2 plasma (150 W) in an Oxford 80Plus reactive ion etcher and finally rinsed in deionized wafer (DIW) before bonding. In both plasma treatments the processing time was 30 s, the chamber pressure was 150 mTorr, and the gas flow was 30 standard cm^3/min.
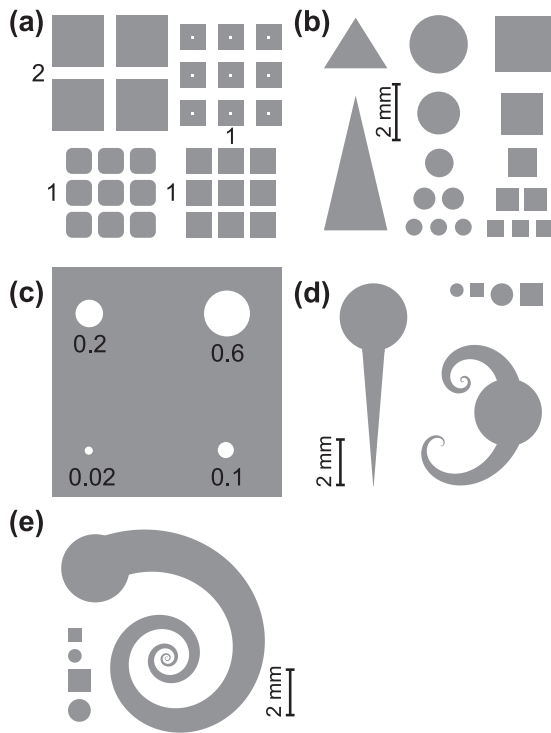
Figure 4. Layouts of (*a*) square recess, (*b*) mixed recess, (*c*) mesa, and (*d*) mixed spiral and (*e*) long spiral bonding test structures. The recessed regions are shown in gray. The lengths and diameters of the structures are shown in millimeters. In (*a*) the radius of curvature of the rounded squares is 100 μm, and the square pillars in the top-right squares are 50 μm wide. The pictures are not in scale.

The details of all experiments are combined in Table I. In general, one bonded wafer pair was fabricated for one combination of the prebonding treatment and the value of h. In both experiment III.S1 and III.D2 two bonded wafer pairs were fabricated. In both III.S2 and III.D1 four bonded wafer pairs were fabricated in two separate processing runs.

All the wafers were bonded in vacuum (10^{-3} mbar) at room temperature (RT) using either EVG5201S (fusion bonded wafers) or EV801 (plasma-activated wafers) wafer bonder (Fig. 6e). In order to see if the local bonding near the test structures changes during bonding, the fusion bonded wafers of experiments III.S and III.D were annealed in a wet oxidation process in two steps: first at 900 °C for 1 hour and then at 1100 °C for 2 hours. The rest of the fusion bonded wafers were annealed at 1100 °C for 2 hours. The plasma-activated wafers were annealed in vacuum at 400 °C for 1 hour.

SAM imaging and bonding test structure analysis.— The acoustic micrographs of the bonded and annealed wafers were obtained using a Sonix HS3000 SAM. Bonded wafers from experiments II.S and II.D were also investigated with SAM before each annealing step. For reference, the bonding strengths of unpatterned wafers (one bonded pair for each type of prebonding treatment) were measured with the crack opening method.[27] Three samples were diced from each test wafer. The result of the crack opening test (COT) is an average value of the surface energies of these samples.

The SAM images were processed and analyzed with MATLAB. Before the analysis the SAM images were enhanced using the blind deconvolution function deconvblind, which also yields the point-spread function (PSF) of the imaging system. The obtained PSF suggests that the spot size of the SAM is around 50 μm, which is in close agreement with manufacturer's specification.

The MATLAB analysis algorithm counts the number of bonded recess test structures on the wafer and measures the widths of the
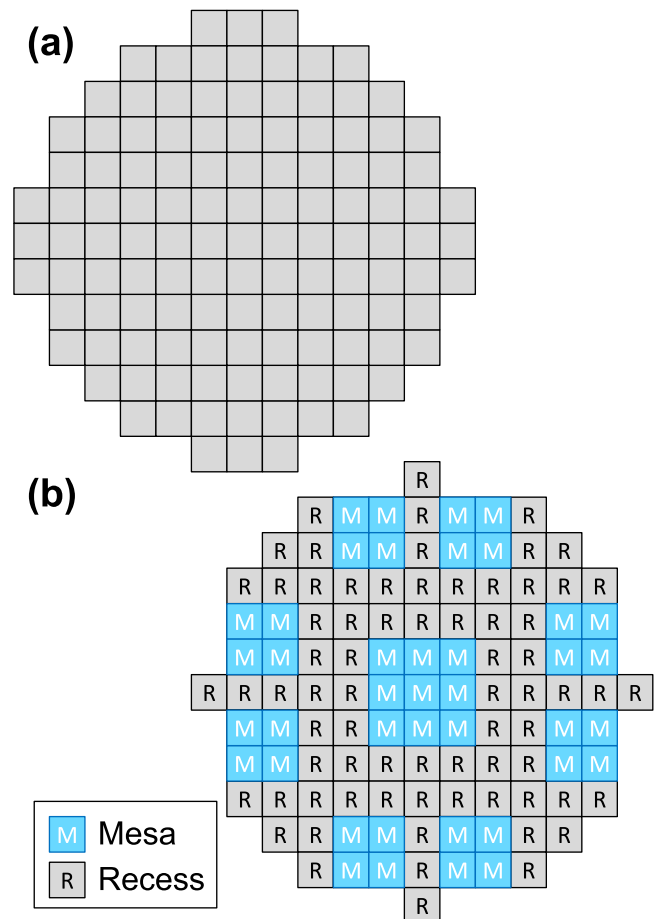
Figure 5. Wafer-level layout arrangements used in the experiments: (*a*) Simple arrangement consisting of 121 layouts of the same type. (*b*) Mixed arrangement consisting of 41 mixed recess (Fig. 4b) and 72 mesa (Fig. 4c) bonding test structures.
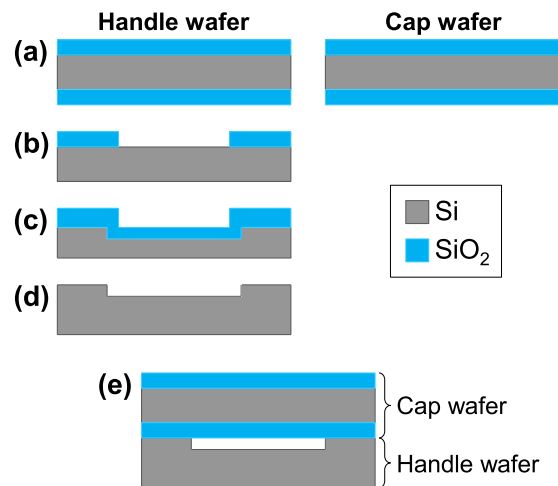
Figure 6. Fabrication steps of the sample wafers: (*a*) Growth of 500 nm of thermal oxide. (*b*) Patterning of the silicon oxide. (*c*) Growth of thin thermal oxide. (*d*) Removal of all oxide, and either SC1 cleaning or plasma activation and rinsing in deionized water. (*e*) Bonding in vacuum at room temperature and annealing. The pictures are schematic and not in scale.

Table I. Details of experiments.

Exper-iment	Wafer pairs	Bond test structure	Wafer-level arrangement	h	Prebonding treatment	Annealing
I.S	1	Square recess (Fig. 4a)	Simple (Fig. 5a)	11 nm	Standard SC1 at 65 °C	1100 °C for 2h
I.D	1	Square recess (Fig. 4a)	Simple (Fig. 5a)	11 nm	Dilute SC1 at 45 °C	1100 °C for 2h
II.S	3	Mixed recess & mesa (Fig. 4b&c)	Mixed (Fig. 5b)	12 nm 16 nm 19 nm	Standard SC1 at 65 °C	900 °C for 1h + 1100 °C for 2h
II.D	4	Mixed recess & mesa (Fig. 4b&c)	Mixed (Fig. 5b)	10 nm 12 nm 16 nm 19 nm	Dilute SC1 at 45 °C	900 °C for 1h + 1100 °C for 2h
III.S1	2	Square recess (Fig. 4a)	Simple (Fig. 5a)	12 nm	Standard SC1 at 45 °C	1100 °C for 2h
III.S2	4	Square recess (Fig. 4a)	Simple (Fig. 5a)	12 nm	Standard SC1 at 65 °C	1100 °C for 2h
III.D1	4	Square recess (Fig. 4a)	Simple (Fig. 5a)	12 nm	Dilute SC1 at 45 °C	1100 °C for 2h
III.D2	2	Square recess (Fig. 4a)	Simple (Fig. 5a)	12 nm	Dilute SC1 at 65 °C	1100 °C for 2h
IV.N	1	Square recess (Fig. 4a)	Simple (Fig. 5a)	12 nm	N₂ plasma*	400 °C for 1h
IV.O	1	Square recess (Fig. 4a)	Simple (Fig. 5a)	12 nm	O₂ plasma*	400 °C for 1h
V.S	1	Mixed spiral (Fig. 4d)	Simple (Fig. 5a)	11 nm	Standard SC1 at 65 °C	1100 °C for 2h
V.D	1	Mixed spiral (Fig. 4d)	Simple (Fig. 5a)	11 nm	Dilute SC1 at 45 °C	1100 °C for 2h
VI.S	1	Long spiral (Fig. 4e)	Simple (Fig. 5a)	11 nm	Standard SC1 at 65 °C	1100 °C for 2h
VI.D	1	Long spiral (Fig. 4e)	Simple (Fig. 5a)	11 nm	Dilute SC1 at 45 °C	1100 °C for 2h

*Standard SC1 at 65 °C before and DIW rinse after the plasma treatment.

unbonded rims of the mesa and recess test structures. Every test structure on the studied bonded wafer pairs was measured and analyzed. The determination of the bonding of the recess test structures is based on the average intensity of the SAM image in roughly 80×80 µm² area inside the test structure. The wafer-level bonding probability of each kind of test structure is calculated from the measured number of specific bonded test structures with the formula

$$\text{Bonding probability} = \frac{\text{Number of bonded test structures}}{\text{Total number of test structures on wafer}}. \quad [10]$$

The length or width of the unbonded region was calculated by first summing up the intensities of all the pixels around the test structures. This sum corresponds to the total unbonded area. Finally, the length or width of the unbonded region is calculated based on this measured area and the known geometry of the test structure. In order to avoid the effect of the corners in the further analysis, the lengths of the unbonded regions of along the sides of the square recess test structures were obtained by taking the average of the average unbonded lengths in 280 µm wide areas at the center of the 4 sides. The apparent surface energies corresponding to the measured dimensions of the unbonded regions were obtained from the surface energies calculated for each test structure using the FEM model (Figs. 8 and 9a).

Results and Discussion

Comparison of surface energies calculated with analytical and FEM models.—The apparent surface energies of two surface step test struc-

tures and two recess test structures are plotted in Fig. 7. The heights and depths of the surface steps and recesses are 10 nm and 15 nm. Generally the apparent surface energies increase with decreasing d_{step} and d_{circ} because the required deformation energy increases when the deformed area decreases at constant step height or recess depth. That is to say, high surface energies induce stronger deformation.

In both cases the present analytical models, Eqs. (4) and (9), and the FEM simulations agree well when the dimensions of the unbonded regions, d_{step} and d_{circ}, are larger than 10 mm. At shorter unbonded regions the present analytical models, Eqs. (4) and (9), yield orders of magnitude higher surface energies than the FEM simulations. The reason for this is that at small dimensions (d_{step} and d_{circ} less than 1 mm) the analytical models based on the thin plate theory overestimate the mechanical energies needed in the deformations. At small dimensions, in fact, the thin plate theory is not valid because the thickness of the wafer should not be more than about 1/4 of the least transverse dimension of the deflected structure.[25] Most of the practical geometries and the test structures utilized in this work violate this assumption as well. In spite of this, the analytical formulas provide still insightful information how the surface energy depends on the geometrical and material parameters.

The analytical model by Martini et al., Eq. (5), agrees with the FEM simulations when $d_{step} \sim 2t$ (see Fig. 7a), but yields 1–3 orders of magnitude lower surface energies when $d_{step} < 2t$. This difference is presumably due to local high stress points at the shoulder corners of the recess test structures. These high stress points, which were seen in the FEM simulations, increase total strain energy U of the structures, thus contributing to higher apparent surface energies. The analytical models are not able to describe these high stress points, but all of
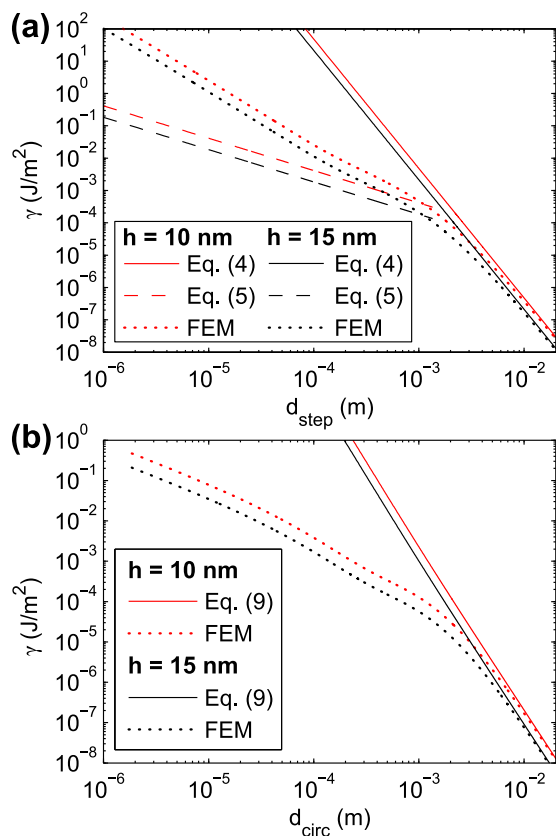
Figure 7. Calculated apparent surface energy γ as a function of (*a*) the length d_{step} of the unbonded region near the surface steps and (*b*) the width d_{circ} of the unbonded rim in the circular recesses with $b = 200\,\mu$m. The height of the step h (a) and the depth of the recess h (b) are varied. The thickness of both wafers are 675 μm. The curves were calculated using the present analytical model (Eq. (4)), the analytical model by Martini et al. (Eq. (5)), and the FEM simulation software together with either Eq. (6) (a) or Eq. (1) (b).

Figure 8. Calculated apparent surface energy γ as a function of the width d_{circ} of the unbonded rim (*a*) in circular recesses with various values of *a* and (*b*) around circular mesas with various values of *b*. The depth of the recessed h and the height of the mesas h are 10 nm. The curves were calculated using the FEM simulation software and Eq. (1) with wafer thickness of 675 μm.

them are able to describe well the h-dependence, $\gamma \propto h^2$, in the whole range of d_{step} and d_{circ}.
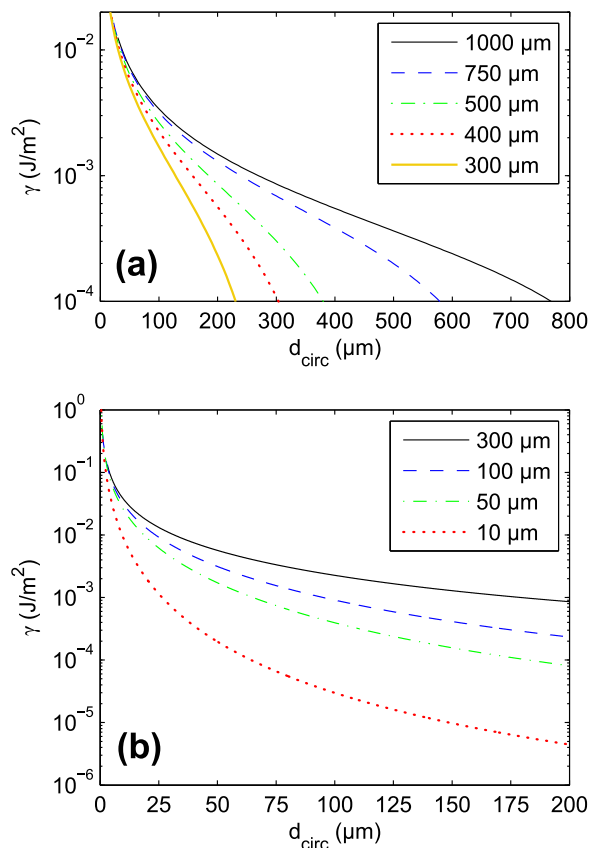
In summary, Fig. 7 shows that the FEM and analytical models of this work agree very well when the dimensions of the test structures are large. When d_{step} and d_{circ} are less than 1 mm, however, only the FEM models can be used since the present analytical models are not valid in this range.

Dependencies of apparent surface energies on bond test structure geometries.—The calculated apparent surface energies of the recess and mesa bonding test structures are plotted in Fig. 8a and b as functions of the width of the unbonded rim. The graphs show that these test structures can be used for measuring the apparent surface energies in the range 10^{-4}–10^{-2} J/m^2.

The apparent surface energies of the surface step bonding test structures are plotted in Fig. 9. The dynamic range of the surface steps extends to as high as 10 J/m^2. Across the range of interest the h-dependencies of the curves in Fig. 9b are extremely close to the h^2-dependency predicted by the analytical models, Eqs. (4) and (5). This was tested by fitting the curve $\gamma = \alpha h^2$, where α is a constant, to the data. The relative root-mean-square (RMS) errors of the fits were only 1–3 ppm. Similar results were obtained also for the mesa and recess structures.

Effect of temperature and dilution of SC1 on fusion bonding.— The effect of standard and dilute SC1 was studied at 45 °C and 65 °C. In general, the use of the lower dilution improved bonding quality at both temperatures, and higher bonding quality was obtained at the

lower temperature regardless of the dilution. Below we focus on the details of the extreme cases.

The unprocessed SAM images of fusion bonded wafers with standard and dilute SC1 cleaning treatments at 65 °C and 45 °C, respectively, are shown in Fig. 10. Most of the large square recesses in the dilute SC1 wafers are bonded in Fig. 10b, whereas in the standard SC1 wafers most of them are not bonded in Fig. 10a. In addition, the narrower unbonded rims in the inset of Fig. 10b are clearly visible.

Maps of the widths of the unbonded rims and the corresponding apparent surface energies obtained from the SAM images using the procedure explained in the experimental section are shown in Fig. 11. Fig. 11 shows that the wafer pair activated in dilute SC1 has much narrower unbonded rims and the corresponding higher apparent surface energies than the wafer pair activated in standard SC1. Also, the variation of the apparent surface energy across the wafer is more uniform in the case of dilute SC1.

In experiments II.S and II.D (see Table I) the wafers were investigated with SAM before and after the annealing steps. These SAM images were closely similar to the SAM images obtained after the annealing. This supports the fact that these kinds bond test structures characterize the bonding interface at the time of wafer contact.[12]

SAM images of the recess and mesa test structures of Fig. 4b and c on fusion bonded wafers are shown in Fig. 12, where differences in the dimensions of the unbonded regions are clearly seen. The average widths of the unbonded regions d_{step} and unbonded rims d_{circ} are plotted in Fig. 13 as functions of the surface step height, mesa height, and recess depth, respectively. The calculated surface energy curves
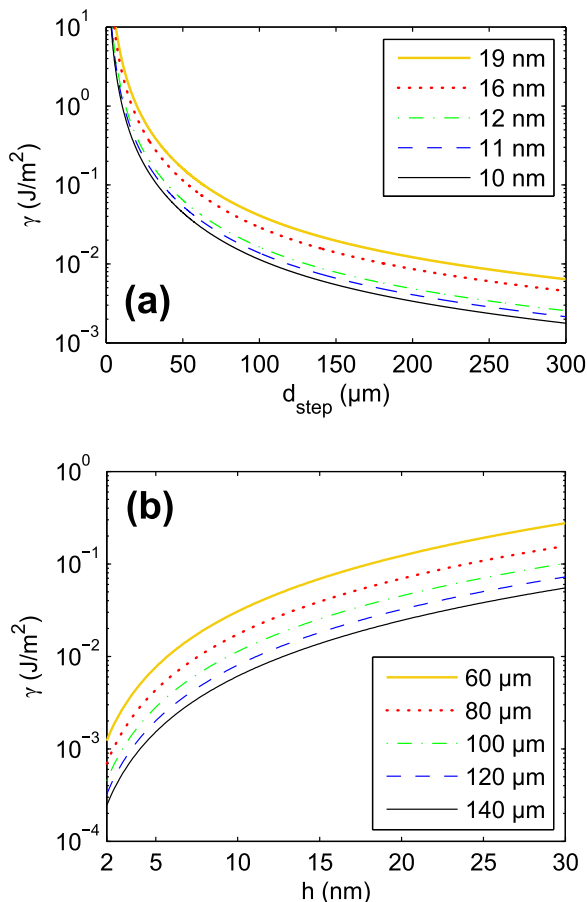
Figure 9. Calculated apparent surface energy γ as a function of (*a*) the length d_{step} of the unbonded region near a surface step and (*b*) the height h of the surface step. h is varied from 10 nm to 19 nm in (*a*) and d_{step} from 60 μm to 140 μm in (*b*), respectively. The curves were calculated using the FEM simulation software and Eq. (6) with wafer thickness of 675 μm.

in Fig. 13 were obtained from the FEM simulations by assuming $\gamma_{step} \propto h^2$ and $\gamma_{circ} \propto h^2$.

Fig. 13 shows that the surface step, mesa, and recess models produce slightly different apparent surface energies from the experimental data. The surface step model estimates the highest apparent surface energies: 12–30 mJ/m^2 for dilute SC1 (45°C) wafers with step height of 10–19 nm, and 13 mJ/m^2 for standard SC1 (65°C) wafers with step height of 12–16 nm. The mesa and recess models estimate lower values: 6–14 mJ/m^2 for dilute SC1 (45°C) wafers with h of 10–19 nm, and 7–9 mJ/m^2 for standard SC1 (65°C) wafers with h of 12–16 nm.

Since the apparent surface energies of the wafers with the same composition and surface treatment should be the same, these results suggest that the present models are not fully applicable in the present experiments. The most probable reason for this is the fact that the present models do not take the 500 nm thick silicon oxide layer into account. However, the present models are still useful in giving estimations of the surface energies. Addition of the oxide into the models needs careful modeling of the stresses originating from the oxidation process. Therefore, further information on these stresses and the details of the oxidation process are needed.

As it has been already shown some of the recesses are bonded and some are not. The bonding probability of a recess depends on the depth, the lateral size, and the shape of the recess as well as the activation treatment of the surfaces. The measured bonding probabilities of circular and square recesses (see Eq. (10) in the experimental section) as functions of the area and the depths of the recesses are shown in Figs. 14 and 15. The bonding probability decreases with increasing
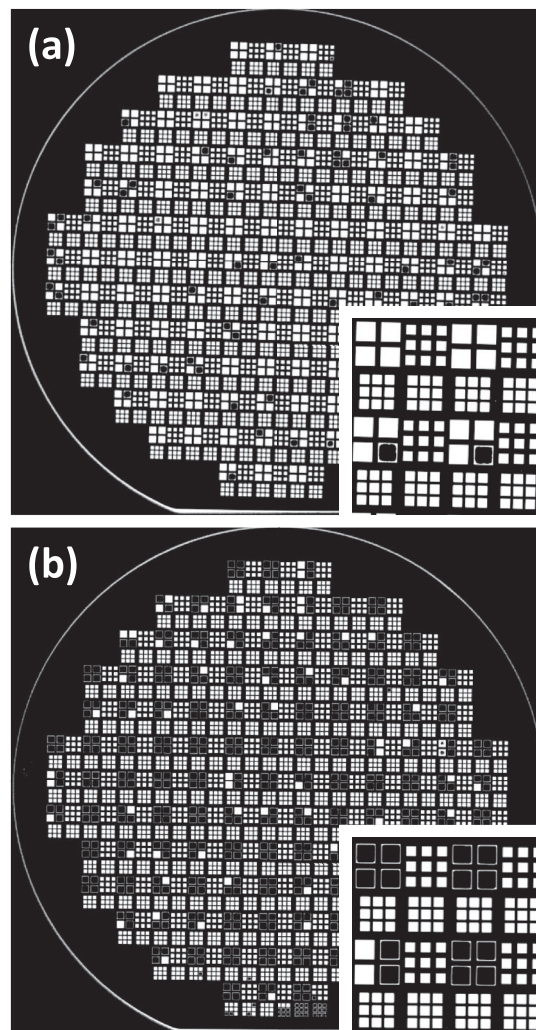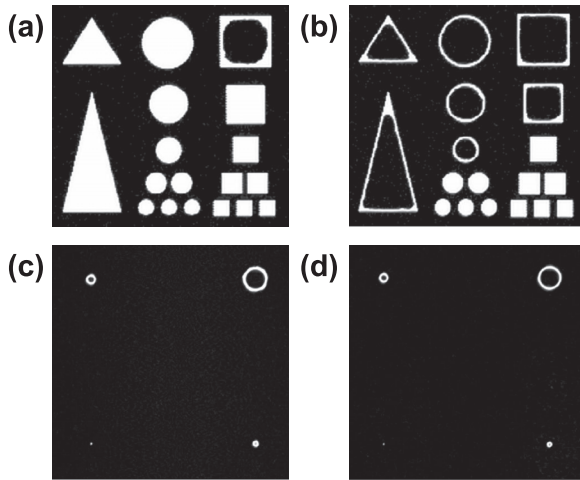

Figure 10. SAM images of fusion bonded wafers I.S and I.D with 11 nm deep recesses shown in Fig. 4a. The wafers were cleaned in (*a*) standard SC1 at 65 °C and (*b*) dilute SC1 at 45 °C. The insets show magnifications of the wafer centers.
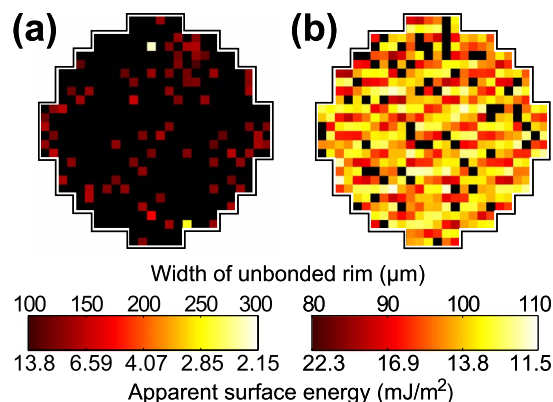
Figure 11. Measured widths of the unbonded rims in the 2000 μm wide and 11 nm deep recesses square recesses in the wafers cleaned in (*a*) standard SC1 at 65 °C and (*b*) dilute SC1 at 45 °C. The data was obtained by deconvolution and analysis of the SAM images of Fig. 10. The corresponding apparent surface energies are also shown. Completely unbonded recesses are shown in black. (*a*) 15.5% and (*b*) 86.4% of these recesses were bonded. The average unbonded rim widths were (*a*) 134.7 μm and (*b*) 98.31 μm.

Figure 12. SAM images of bond test structures of (*a,b*) Fig. 4b and (*c,d*) Fig. 4c on fusion bonded wafers with 12 nm deep recesses (experiments II.S and II.D). The wafers were cleaned in (*a,c*) standard SC1 at 65 °C (II.S) and (*b,d*) dilute SC1 at 45 °C (II.D).

recess depth and increases with increasing recess size. The shape has a minor effect on the probability, at least in the case of squares and circles. The surface treatment has a huge impact on the bonding: The bonding probability of a 2 mm wide and 12 nm deep square recess is 71.8 % on a wafer cleaned in dilute SC1 at 45 °C and 12.7 % on a wafer cleaned in standard SC1 at 65 °C (see Fig. 14).

This statistical problem of recess bonding is similar to the yield problem in integrated circuit (IC) manufacturing: In IC manufacturing local, stochastic defects on wafers cause failures of some of the manufactured ICs. In this work, local, stochastic features on wafer surfaces cause bonding of some recesses. Therefore, yield models[28,29,30] can be used to describe the probability of a bond initiation site being found in a recess. It should be also noted that kinetic models cannot be used here, because there is no equilibration process: The bonding of the recesses is a fast process which stops after the bonding front has passed the recesses. The early phases of the wafer bonding process can be described by models initially developed for stiction in MEMS.[31,32] In general, the interaction between the bonding surfaces is determined by capillary forces, van der Waals forces, electrostatic forces and forces related to hydrogen and solid bridging.[31,32] It is very unlikely, however, that capillary forces play a role in vacuum bonding of recesses. In addition to the environmental conditions such as temperature, the roughness of the bonding surfaces has profound effect on the bonding process.

In the yield models, the yield Y of the fabricated devices is limited by defects. In the present problem, however, there are local disturbances on wafers, which cause the bonding of recesses to occur. In the context of a yield model, the defects themselves cause the bonding. Therefore, the probability of a recess to bond can be written as $1 - Y$.

We analyzed the data of Fig. 14 with two general models, the negative binomial model[28,29] and the variable defect size (VDS) model.[30] These yield models are able to explain the behavior of the 10 nm deep recesses with areas higher than 1.5 mm². The VDS model suggest that the bonding is caused by a point-like sources with a density of 0.9 mm⁻². These models and the other common yield models,[28,29,30] however, predict much higher probabilities than observed when the recess area is smaller than 1.5 mm². This discrepancy is even higher with deeper recesses and the standard SC1 cleaning. The discrepancy is most likely because these models do not take the energy needed to bond into account. In general, the density of the initial energy needed for the recess to bond increases with decreasing recess area simply due to the fact that the bonding of smaller recesses must begin with smaller value of d_{circ} (see Fig. 7b). Presumably, the limited availability
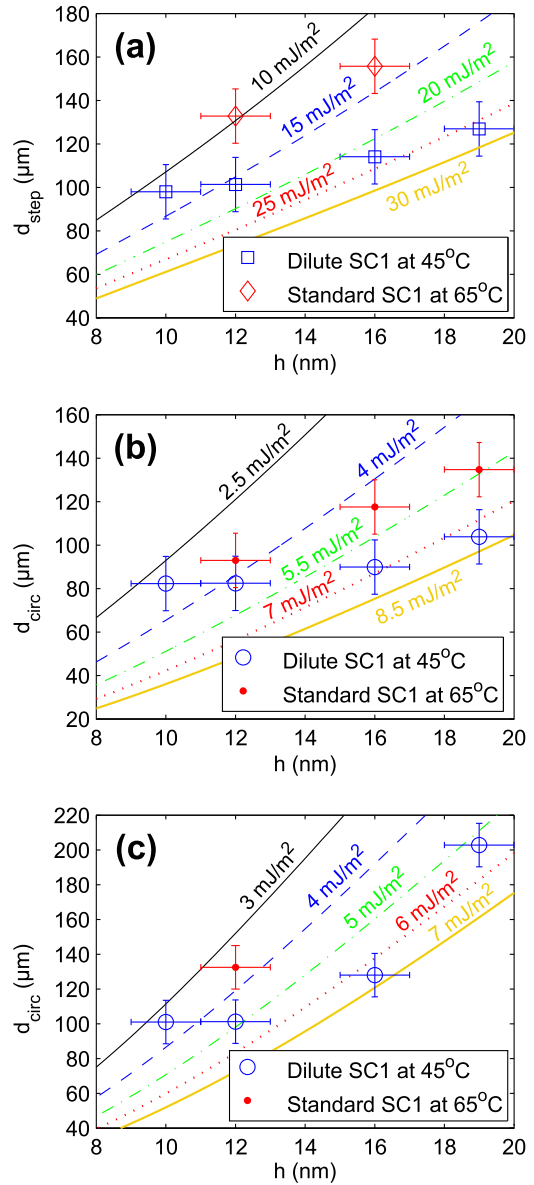

Figure 13. Measured wafer-level values of (*a*) average d_{step} of a surface step (from 2000 μm wide square recesses), (*b*) average d_{circ} of a 600 μm circular mesa, and (*c*) average d_{circ} of a 2000 μm circular recess as a function of h. Two different SC1 treatments are compared (experiments II.S and II.D). Lines are calculated constant apparent surface energies. Each data point represents average of (*a*) 41, (*b*) 72, and (*c*) 41 test structures on a single wafer.

of energy during the bonding process reduces the bonding probability if the required energy is high.

Fig. 16 shows the dependence of the width of the unbonded rim of the 2000 μm square recesses on the bonding probability of the same recess. There is a clear dependence between these two: When the unbonded width is small, the bonding probability is large and vice versa. Since the width of the unbonded rim is inversely proportional to the apparent surface energy, this suggests, rather obviously, that the bonding probability of a recess increases with increasing apparent surface energy of the bonding surface. This effect is also clearly visible in Fig. 10.

The experimental data in Fig. 16 shows that the apparent surface energy of the SC1 treated surfaces decreases in the order 1) dilute SC1 at 45°C, 2) standard SC1 at 45°C, 3) dilute SC1 at 65°C, and 4) standard SC1 at 65°C. The data suggests that as the strength of the SC1 mixture increases, the apparent surface energy decreases.
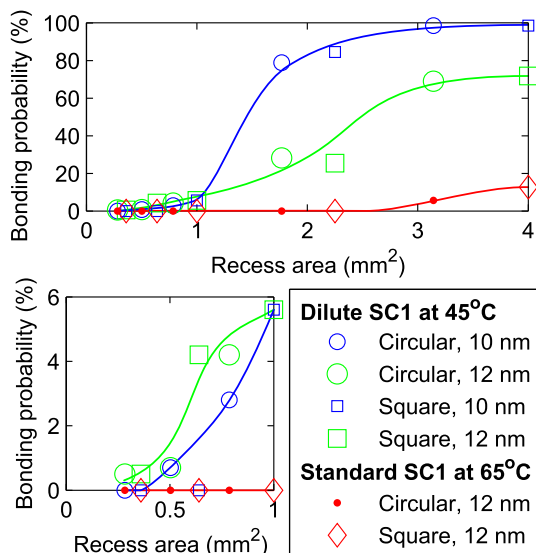
Figure 14. Measured wafer-level bonding probabilities of circular and square recesses as functions of the area of the recess and the varying recess depths and SC1 treatments (experiments II.S and II.D). The bottom graph shows a magnification of the upper graph. Lines guide the eye.

These results can be explained by the fact that the surface roughness increases as the NH$_4$OH concentration in the SC1 solution increases.[11]

The SC1 results are summarized in Fig. 17, which also shows the results obtained with the COT. Although COT measures the surface energy as the mechanical energy needed to pull the bonded wafers apart, both apparent surface energy (Fig. 17b) and the recess bonding probability (Fig. 17c) correlate well with the final bond strength of the SC1-treated wafers measured by COT (Fig. 17a). Fig. 17 shows also the results from the plasma-activated wafers, which are discussed in detail in the next section. The apparent surface energy and the recess bonding probability are both measures of the bonding surfaces at the time when the wafers are first brought into contact. The further bonding mechanisms taking place during annealing determine the final bond strength. Because the mechanisms of plasma bonding differentiate remarkably from those in the fusion bonding, the fusion and plasma bonding results in Fig. 17 cannot be directly compared.
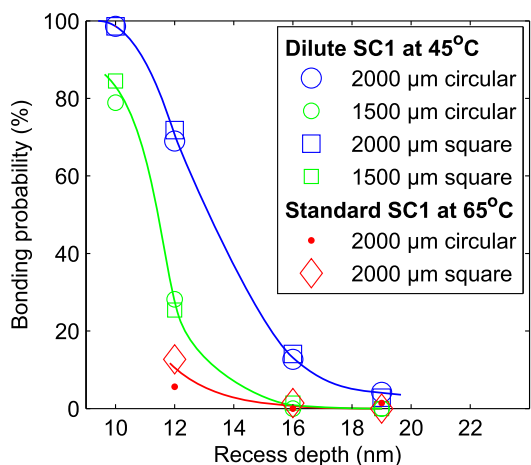

Figure 15. Measured wafer-level bonding probabilities of circular and square recesses as functions of the depth of the recess h and varying diameters of the recesses and SC1 treatments (experiments II.S and II.D). Lines guide the eye.
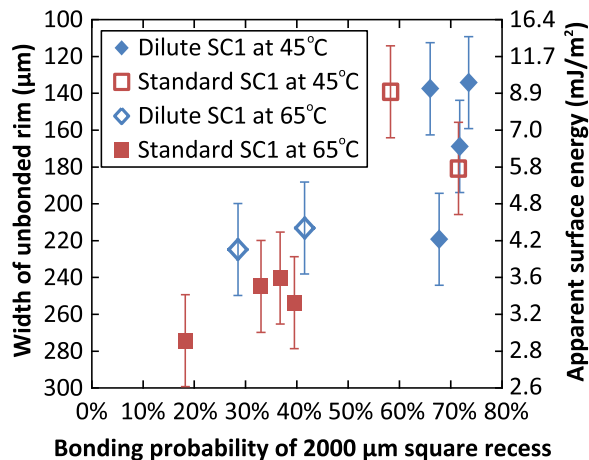

Figure 16. Measured width of the unbonded rims of the 2000 μm wide and 12 nm deep square recesses on bonded wafers treated in SC1 with various dilutions and temperatures (experiments III.S1, III.S2, III.D1, and III.D2) as functions of the measured wafer-level bonding probabilities. The corresponding apparent surface energies are also shown. Each data point corresponds to a single test structure on an individual wafer. The unbonded rims of typical recesses were measured manually with a high-resolution SAM scan.

Overall, the estimation of surface energy based on the measured bonding probability is, indeed, a fast and simple way to compare cleaning treatments, but does not allow mapping of surface energy and cannot be quantified without reference samples. The results imply that the surface energy at the time the wafers are brought into contact
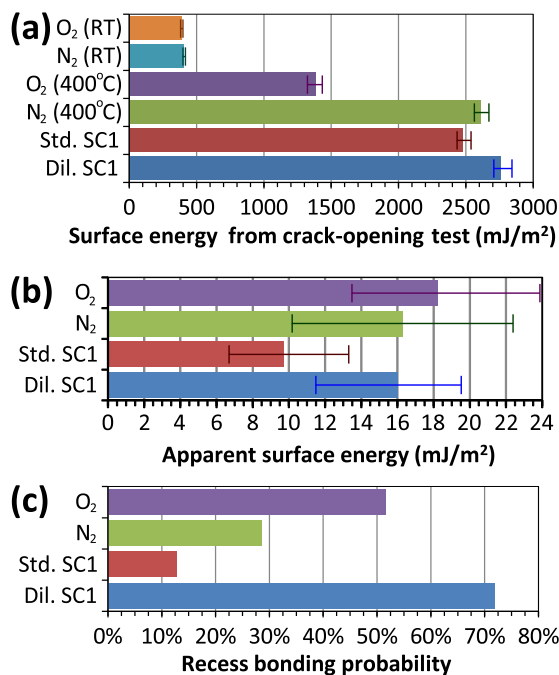
Figure 17. Comparison of results from fusion bonded and plasma-activated wafers: (*a*) surface energies measured using the crack-opening test (COT), (*b*) the apparent surface energies obtained from the bonding test structures (Figs. 11 and 19), and (*c*) the bonding probabilities of 11 nm (SC1) and 12 nm (O$_2$ and N$_2$ plasma) deep recesses (Figs. 11 and 19). The values are measured averages of (*a*) 3 samples from a single wafer pair and (*b,c*) 121 test structures on a single wafer. The standard SC1 cleaning was performed at 65°C and the dilute SC1 at 45°C. The COT surface energies of the SC1-treated wafers were measured after annealing at 1100°C for 2h, whereas the O$_2$ and N$_2$ plasma-activated wafers were measured directly after bonding at room temperature (RT) and after annealing at 400°C for 1 h.
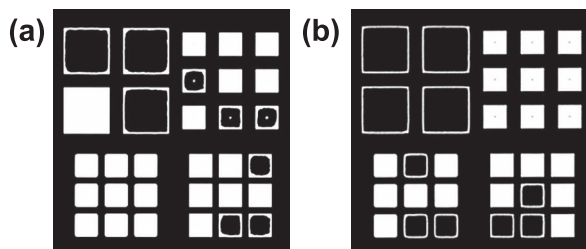
Figure 18. SAM images of bond test structures of Fig. 4a on plasma bonded wafers with 12 nm deep recesses (experiments IV.N and IV.O). The wafers were activated in (*a*) nitrogen (IV.N) and (*b*) oxygen plasma (IV.O).

determines also the final bond strength of SC1-treated wafers which is obtained after annealing.

Comparison of nitrogen and oxygen plasma activated samples.— Examples of SAM images of plasma activated wafers are shown in Fig. 18. Maps of the widths of the unbonded rims and the corresponding apparent surface energies obtained from SAM images (see the experimental section) are shown in Fig. 19. Compared to the recesses on the fusion bonded wafers (see Fig. 11) the number of bonded recess on the plasma activated wafers increases toward the edges of the wafers. This could be caused by the spatial variation of the plasma in the processing chamber.

Fig. 17 shows the comparison of the SC1 and plasma activated wafers as well as the bond strength of the plasma-activated wafer measured with COT both before and after annealing. Both plasma-activated wafers have apparent surface energies near 20 mJ/m², which are in agreement with the values 40–75 mJ/m² reported by Bodner et al.[33] The results in Fig. 17 suggest that the surface energy and the resulting interaction of the bonding surfaces is stronger in O$_2$ plasma activated wafers than in N$_2$ plasma activated wafers and even SC1-treated wafers, but this does not turn into high bond strength during annealing. In the case of nitrogen plasma, strong final bond strength is obtained during annealing in spite of weaker interaction. Compared to the fusion bonding of the SC1-treated wafers, differences between the interaction of the bonding wafers can also explain the fact that the apparent surface energy and the recess bonding probability of the plasma-activated wafers are only slightly correlated with the COT surface energies measured at RT and not correlated with the COT surface energies measured after annealing.
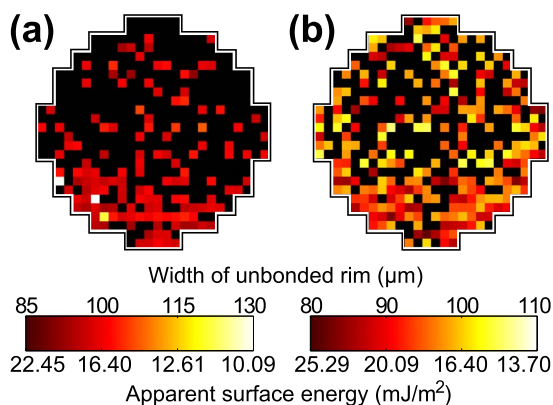
Figure 19. Measured widths of the unbonded rims in the 2000 μm wide and 12 nm deep square recesses in the wafers activated in (*a*) nitrogen and (*b*) oxygen plasma (experiments IV.N and IV.O). The corresponding apparent surface energies are also shown. Completely unbonded recesses are shown in black. (*a*) 28.5% and (*b*) 51.7% of these recesses were bonded. The average unbonded rim widths were (*a*) 100.2 μm and (*b*) 95.3 μm.

Whereas the SC1-treated samples allow a straightforward interpretation of apparent surface energy in terms of surface roughness, the plasma activated wafers are not so simple. As Fig. 17 shows the apparent surface energy of the N$_2$ activated surface is comparable to that of the SC1 activated surfaces. The O$_2$ activated surface is even higher. This contrasts with the typical expectation, confirmed here as well, that the bond strength of the N$_2$ and O$_2$ activated wafers after annealing are often lower than that of the SC1-activated fusion bonded pairs. Furthermore, O$_2$ activated pairs should be weaker than N$_2$ bonded pairs. The discrepancy in the behavior of SC1 activated and plasma activated surfaces may lie in the nature of the surfaces created.

The surface energy of a solid has both polar and non-polar components. A perfect, defect free oxide surface comprised of bridging oxygen atoms is effectively hydrophobic. A fresh, thermal oxide provides an example of an oxide surface with a relatively high contact angle (hydrophobic)[34] with a surface covered mainly in siloxanes.[35] Introduction of defects will increase the surface energy toward hydrophilic behavior. Non-bridging oxygen atoms have been modeled on such surfaces.[36] Wendt and co-workers[37] noted that water will adsorb molecularly on defect free silica, but dissociatively on silica with surface defects, implying that the defect-free surface will lack polar components. M. Chassé and G. G. Ross[38] studied Ar ion implanted silicon surfaces. Their results show, similarly as ours, that the presence of oxygen during Ar treatment increases the surface energies of the samples. M. Chassé and G. G. Ross explained this to be due to the removal of hydrocarbons.[6,38]

Both N$_2$ and O$_2$ plasma activation processes are expected to create defects on the surfaces. If the O$_2$ activated surface is systematically richer in complex oxygen-related defects (beyond those found on the N$_2$ activated surface), then that could explain the higher apparent surface energy of the O$_2$ activation process. It has also been speculated,[39] that some of the oxygen related defects are not amenable to the low temperature reactions needed to achieve high bond strength. Therefore, whereas the O$_2$ plasma treated surface possesses a high-energy, as measured here, the nature of the defects may impede the bonding reactions between the joining wafer surfaces.

Advanced recess bonding test structures.— During the experiments we observed that the tip of the large triangle shown in Fig. 4b was very sensitive to the local bonding conditions (see also Fig. 12b). In the case of 10 nm deep recesses and cleaning in dilute SC1 at 45 °C (experiment II.D), the length of the unbonded region at the tip varied from 236 to 1888 μm with the average value of 839 μm. Only 4 large triangles were bonded in wafers cleaned in standard SC1 at 65 °C (experiment II.S). The average unbonded width was 1091 μm and the range from 309 μm to 1818 μm.

In order to fully exploit this phenomenon, we designed new test structures with long and sharp features. The layouts of these test structures are shown in Fig. 4d and e. The spiral shape allows long shapes to be confined locally, thus it increases the dynamic range of the test structure remarkably. A triangle and two spirals with equal lengths are compared in the layout of Fig. 4d. The test structures are connected to a large circular recess in order to ensure initiation of the bonding.

The SAM images of these structures are shown in Fig. 20. The test structures act as gauges: The longer the bonding front (shown in black) extends into the tip of the spiral or the triangle, the better the bonding strength. Fig. 20a and b show that the shorter triangle and spirals produce similar results, but their dynamic range is not wide enough for the wafers cleaned standard SC1 at 65 °C. The longer spiral of Fig. 4e has wide enough dynamic range for the wafers cleaned in both types of SC1. Fig. 20c shows also that the apparent surface energies indicated by the test structures can be slightly different in different locations on the wafer. This allows SAM imaging and image analysis to be used to perform mapping of the apparent surface energy on the wafers.
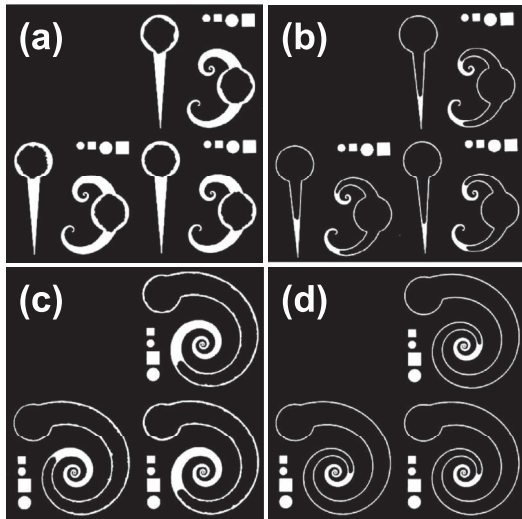
Figure 20. SAM images of spiral bonding test structures of Fig. 4d and e on fusion bonded wafer pairs from experiments (*a*) V.S, (*b*) V.D, (*c*) VI.S, (*d*) VI.D. The bonded wafers were cleaned in (*a, c*) standard SC1 at 65 °C and (*b, d*) dilute SC1 at 45 °C.

Conclusions

We have presented a method for measurement of apparent surface energy of cleaned wafer surfaces locally utilizing either recess or mesa bond test structures, SAM, image processing and analysis, and FEM analysis. It allows local mapping of the apparent surface energy across the bonded wafer pair. We have also presented an alternative, statistical method to determine the average surface energy at the wafer level from the measured bonding probability of shallow recess bond test structures. The bonding probability gives also information on the interaction between the wafer surfaces. Results from both methods correlate with each other. The present methods allow the evaluation of surface cleans without destructive, off-line methods such as the crack-opening method.

The results obtained with the present methods and the crack-opening method show that the bond strength of the annealed wafers depend on the pre-bonding activation and increase in the order 1) O_2 plasma, 2) standard SC1 at 65 °C, 3) N_2 plasma, and 4) dilute SC1 at 45 °C. In addition, the results imply that the local bonding near a step and the wafer level bonding probability are correlated and governed by the surface energy at the time the wafers are brought into contact. In the case of SC1-activated fusion bonding this surface energy is also proportionally converted into the final bond strength obtained after annealing. As the mechanism of O_2 and N_2 plasma-activated wafer bonding is different, this correlation of the apparent surface energy and bonding probability with the final bond strength was not observed in O_2 and N_2 plasma activated wafers.

The results of this work can also be used in the fabrication of shallow cavities and bonding of wafers with recesses. When dilute SC1 cleaning is used at 45 °C, the cavity will not collapse if the cavities are deeper than 25 nm and the lateral area of a circular or square cavity is less than 2 mm^2. Our results show that wafers with circular or square recesses bond with 100% certainty if the recesses are shallower than 8 nm and their area is larger than 4 mm^2. When standard SC1 cleaning is used at 65 °C, the values for shallow cavities are the same as with the dilute SC1, but guaranteed bonding of wafers with recesses cannot be estimated based on our data. Between these extremes, the bonding of various cavity sizes and depths obey a probabilistic trend.

Finally we have proposed advanced test patterns, which allow in-line monitoring of the surface clean effectiveness on process wafers. As the methods and test patterns employed in this work are not limited to Si/SiO$_2$ bonding, we are confident that they are useful also in the study of the bonding and interaction of other surfaces as well.

References

1. M. Alexe and U. Gösele, *Wafer Bonding: Applications and Technology*, Springer-Verlag, Berlin, Germany (2004).
2. S. Franssila, *Introduction to Microfabrication*, John Wiley & Sons, West Sussex, England (2004).
3. A. Plößl and G. Kräuter, *Mater. Sci. Eng., R*, **25**, 1 (1999).
4. H. Moriceau, F. Rieutord, C. Morales, S. Sartori, and A. M. Charvet, Surface Plasma Activation Before Direct Wafer Bonding: A Short Review and Recent Results, in K. D. Hobart, S. Bengtsson, H. Baumgart, T. Suga, and C. E. Hunt (eds.), *Semiconductor Wafer Bonding VIII: Science, Technology, and Applications*, The Electrochemical Society, Inc., Pennington, New Jersey, pp. 34-49 (2005).
5. S. N. Farrens, J. R. Dekker, J. K. Smith, and B. E. Roberds, *J. Electrochem. Soc.*, **142**(11), 3949 (1995).
6. R. H. Esser, K. D. Hobart, and F. J. Kub, *J. Electrochem. Soc.*, **150**(3), G228 (2003).
7. P. Ericsson and S. Bengtsson, *J. Electrochem. Soc.*, **143**(11), 3722 (1996).
8. Q.-Y. Tong and U. Gösele, *Semiconductor Wafer Bonding: Science and Technology*, Wiley-Interscience, New York (1999).
9. W. P. Maszara, G. Goetz, A. Caviglia, and J. B. McKitterick, *J. Appl. Phys.*, **64**(10), 4943 (1988).
10. M. Itano and T. Kezuka, in *Ultraclean Surface Processing of Silicon Wafers* T. Hattori, Editor, p. 40, Springer-Verlag, Berlin (1998).
11. T. Ohmi, M. Miyashita, M. Itano, T. Imaoka, and I. Kawanabe, *IEEE Trans. Electron Devices*, **39**(3), 537 (1992).
12. Ö. Vallin, K. Jonsson, and U. Lindberg, *Mater. Sci. Eng., R*, **50**, 109 (2005).
13. N. Poduje, W. Kerr, and K. T. Turner, *ECS Trans.*, **33**(4), 537 (2010).
14. R. D. Horning, D. W. Burns, and A. I. Akinwande, in *Proceedings of the First International Symposium on Semiconductor Wafer Bonding: Science, Technology and Applications*, p. 386. The Electrochemical Society (1992).
15. D. Pasquariello and K. Hjort, *J. Electrochem. Soc.*, **147**(6), 2343 (2000).
16. T. Martini, S. Hopfe, S. Mack, and U. Gösele, *Sens. Actuators*, **75**, 17 (1999).
17. R. Knechtel, M. Knaup, and J. Bagdahn, *Microsyst. Technol.*, **12**, 462 (2006).
18. S. Tatic-Lucic, J. Ames, B. Boardman, D. McIntyre, P. Jaramillo, L. Starr, and M. Lim, *Sens. Actuators, A*, **60**, 223 (1997).
19. J. A. Plaza, J. Esteve, and E. Lora-Tamayo, *J. Electrochem. Soc.*, **144**(5), L108 (1997).
20. J. A. Plaza, J. Esteve, and E. Lora-Tamayo, *Sens. Actuators, A*, **60**, 176 (1997).
21. J. A. Plaza, J. Esteve, and E. Lora-Tamayo, *Sens. Actuators, A*, **67**, 181 (1998).
22. A. Varpula, J. R. Dekker, and T. Suni, in *Proceedings of 2012 3rd IEEE International Workshop on Low Temperature Bonding for 3D Integration (LTB-3D)*, p. 193, IEEE (2012).
23. K.-T. Wan, R. G. Horn, S. Courmont, and B. R. Lawn, *J. Mater. Res.*, **8**(5), 1128 (1993).
24. K. Hiller, *Ein Beitrag zum direkten bonden mikromechanischer Bauteile*, PhD thesis, TU Chemnitz-Zwickau (1993).
25. W. C. Young and R. G. Budynas, *Roark's Formulas for Stress and Strain*, 7th ed., McGraw-Hill, (2002).
26. V. L. Indenbom and J. Lothe, *Elastic strain fields and dislocation mobility*, p. 54, North-Holland, Amsterdam (1992).
27. R. L. Puurunen, T. Suni, O. M. E. Ylivaara, H. Kondo, M. Ammar, T. Ishida, H. Fujita, A. Bosseboeuf, S. Zaima, and H. Kattelus, *Sens. Actuators, A*, **188**, 268 (2012).
28. M. Raghavachari, A. Srinivasan, and P. Sullo, *Microelectron. Reliab.*, **37**(4), 565 (1997).
29. N. Kumar, K. Kennedy, K. Gildersleeve, R. Abelson, C. M. Mastrangelo, and D. C. Montgomery, *Int. J. Prod. Res.*, **44**(23), 5019 (2006).
30. C. N. Berglund, *IEEE Trans. Semiconductor Manufacturing*, **9**(3), 447 (1996).
31. W. M. Van Spengen, R. Puers, and I. De Wolf, *J. Adhes. Sci. Technol.*, **17**(4), 563 (2003).
32. W. M. Van Spengen, R. Puers, and I. De Wolf, *J. Micromech. Microeng.*, **12**, 702 (2002).
33. T. Bodner, A. Behrendt, E. Prax, and F. Wiesbrock, *Monatsh. Chem.*, **143**(5), 717 (2012).
34. H. F. Okorn-Schmidt, *IBM J. Res. Dev.*, **43**(3), 351 (1999).
35. F. Tardif, A. Chabli, A. Danel, N. Rochat, and M. Veillerot, *J. Electrochem. Soc.*, **150**(6), G333 (2003).
36. V. A. Bakaev, W. A. Steele, T. I. Bakaeva, and C. G. Pantano, *J. Chem. Phys.*, **111**(21), 9813 (1999).
37. S. Wendt, M. Frerichs, T. Wei, M. S. Chen, V. Kempter, and D. W. Goodman, *Surf. Sci.*, **565**, 107 (2004).
38. M. Chassé and G. G. Ross, *J. Appl. Phys.*, **92**(10), 5872 (2002).
39. S. Verhaverbeke, U.S. patent 7314854 (2008).